RSC Advances

RSC Publishing

PAPER

View Article Online
View Journal | View Issue

Cite this: *RSC Advances*, 2013, **3**, 14413

Hierarchical TiO_2 nanobelts@MnO_2 ultrathin nanoflakes core–shell array electrode materials for supercapacitors†

Yongsong Luo,‡[abe] Dezhi Kong,‡[ab] Jingshan Luo,[a] Shi Chen,[a] Deyang Zhang,[b] Kangwen Qiu,[b] Xiaoying Qi,[c] Hua Zhang,[c] Chang Ming Li[d] and Ting Yu*[aef]

Received 6th May 2013,
Accepted 29th May 2013

DOI: 10.1039/c3ra42229a

www.rsc.org/advances

Hierarchical TiO_2 nanobelts@MnO_2 ultrathin nanoflakes core–shell arrays (TiO_2@MnO_2 NBAs) have been fabricated on a Ti foil substrate by hydrothermal approach and further investigated as the electrode for a supercapacitor. Their electrochemical properties were examined using cyclic voltammetry (CV), galvanostatic charge–discharge, and electrochemical impedance spectroscopy (EIS) in a three-electrode cell. The experimental observations clearly show that the fabricated TiO_2@MnO_2 NBAs electrode possesses superior rate capability and outstanding cycling performance due to its rationally designed nanostructure. A specific capacitance as high as 557.6 F g^{-1} is obtained at a scan rate of 200 mV s^{-1} (454.2 F g^{-1} at a current density of 200 mA g^{-1}) in 1 M Na_2SO_4 aqueous solution. The energy density and power density measured at 2 A g^{-1} are 7.5 Wh kg^{-1} and 1 kW kg^{-1} respectively, demonstrating its good rate capability. In addition, the composite TiO_2@MnO_2 NBAs electrode shows excellent long-term cyclic stability. The fabrication method presented here is facile, cost-effective and scalable, which may open a new pathway for real device applications.

1. Introduction

In response to rapidly increasing global energy consumption coupled with the critical issue of climate change, developing and refining a sustainable and renewable energy future has been one of the primary focuses for scientists and engineers worldwide.[1] The exploitation of alternative and green energy sources (such as solar, wind, tide, *etc.*) demands efficient support of energy storage/conversion devices that can compensate for their intermittent characteristics. In general, the energy storage systems for renewable sources must meet several requirements, such as high energy density, high power density, good safety, long cycle life and low-cost.[2] Among various energy storage systems, lithium ion batteries and supercapacitors are the two key leading systems. Up to now, virtually all portable electronics rely on lithium ion batteries, which can store large amounts of energy in a lightweight and compact structure and meanwhile provide suitable power levels for certain applications. However, the ever-growing market for electrical vehicles demands energy systems with fast charge and discharge rates and high power densities, which are the weak points of lithium ion batteries. Compared with lithium ion batteries, supercapacitors as a new class of energy storage device, have attracted intense attention, mainly due to their higher power density, faster charging and discharging within short time, superior cycle lifetime, and higher reliability.[3–5] The performance of supercapacitors greatly depends on their electrode materials. Nanostructured electrodes show great advantages over their bulk counterparts, owing to their high surface area, especially for three-dimensional nanostructure composites, which have been considered as one of the most promising electrode materials due to their short transport pathways for electrons and ions.[6,7]

There are mainly three types of electrode materials for supercapacitors: carbonaceous materials,[8] conducting polymers,[9] and metal oxides/hydroxides.[10] Carbon-based materials store charge electrostatically from the reversible adsorption of ions onto their surfaces, leading to a high power delivery. By contrast, metal oxides/hydroxides and conducting polymers store charge in a faradic or redox-type process similar to

[a]*Division of Physics and Applied Physics, School of Physical and Mathematical Sciences, Nanyang Technological University, 637371, Singapore. E-mail: yuting@ntu.edu.sg*
[b]*Department of Physics & Electronic Engineering, Xinyang Normal University, Xinyang 464000, P. R.China*
[c]*School of Materials Science and Engineering, Nanyang Technological University, 639798, Singapore*
[d]*Institute for Clean Energy and Advanced Materials, Southwest University, Chongqing 400700, P. R China*
[e]*Energy Research Institute at Nanyang Technological University (ERIAN), 639789 Singapore*
[f]*Department of Physics, Faculty of Science, National University of Singapore, 117542 Singapore*

† Electronic supplementary information (ESI) available. See DOI: 10.1039/c3ra42229a

‡ These authors contribute equally to this work.

batteries, which could result in the higher specific capacitance of the active materials.[11] Regardless of the type of electrode material, combining the advantages of different materials to form composites should be an effective way to enhance their supercapacitor performance. Due to its low cost, abundance, environmentally friendly nature and high capacitance, MnO_2 has been intensively investigated as an electrode material for supercapacitors in recent years.[12–14] More significantly, MnO_2-based nanocomposites are usually used in neutral aqueous electrolytes, which can meet the requirements of a ''green electrolyte'' in supercapacitors.[15] The charge storage mechanism for MnO_2 in supercapacitors are widely accepted to be based on redox reactions, which can be separated into (1) the surface adsorption of electrolyte cations, for example, X^+ (X = Li, Na, K, or H_3O), $(MnO_2)_{surface} + X^+ + e^- \leftrightarrow (MnOOX)_{surface}$ and (2) the intercalation/de-intercalation of alkali cations in the bulk, for example, $MnO_2 + X^+ + e^- \leftrightarrow (MnOOX)$.[16,17] However, the low surface area and poor electronic conductivity of MnO_2 remain a major problem. To improve its performance, nearly all approaches are focused on the use of conductive supports, forming MnO_2–conductive matrix hybrid nanostructures.[18] High rate capability and cycling stability could be achieved by reducing the loading of active materials on the conductive supports. Unfortunately, this will result in a low energy density. Thus, various efforts have been made to combine two kinds of active materials together to increase the loading of active materials and surface area. However, their electrochemical performance was largely unsatisfactory due to the lack of well defined micro-/nano-structures and understanding of their synergistic effects.[14,19] To overcome the issues mentioned above, various metal oxide-based nanocomposites with different geometrical attributes and morphological forms have been employed as electrodes for supercapacitors.[20–22] For instance, TiO_2@RuO_2, TiO_2@α-Fe_2O_3, Co_3O_4@MnO_2 and SnO_2@MnO_2 nanocomposites have been developed with improved alkali cation insertion performance.[11,23–26] Moreover, hierarchical nanostructures have also aroused great interest in different research fields due to their highly active surface/interface and robust stability.[27–32] Electrode materials with a hierarchical nanoarchitecture can not only provide the multiple large contact area, but also allow fast cation transport between the electrolyte and the electrode.[33] Thus, a rationally designed integrated architecture, in which each component's properties can be optimized, fast ion and electron transfer is guaranteed and synergistic effects result, is highly promising.

In this paper, hierarchical TiO_2@MnO_2 NBAs are designed as the electrode for supercapacitors. The unique hierarchical nanostructure is expected to manifest greatly improved electrochemical performance due to the integration of the advantages of both TiO_2 and MnO_2. First, the ultrathin MnO_2 nanoflakes are grown and well dispersed on the TiO_2 nanobelts, significantly enhancing the surface area of the electrode. Second, the core–shell nanostructure is beneficial to the electrochemical capacity and cycling stability of the electrode due to the high theoretical capacity of the MnO_2 shell and low volume change of the TiO_2 core. Third, the longitudinally grown TiO_2 nanobelts serve as both the backbone and conductive pathway for the MnO_2 nanoflakes, providing robust support and efficient charge transport. Last but not the least, both the core and shell materials are abundant, low cost, and environmentally benign. As a consequence, we have tested the hierarchical TiO_2@MnO_2 NBAs as the electrode for supercapacitors. Due to the advantages discussed above, the composite TiO_2@MnO_2 NBAs electrode exhibits good rate capability, excellent cycle performance, and highly reversible capacity in 1 M Na_2SO_4 aqueous solution. Therefore, this novel electrode design is not only useful as the desired functions of each constituent can be effectively utilized, but also a strong synergistic effect can be realized. As a result, the TiO_2@MnO_2 NBAs exhibit a high capacitance (about 5 to 10-fold increase) in areal capacitance with respect to pristine TiO_2 NBs. Undoubtedly, these composite TiO_2@MnO_2 NBAs are highly promising for application in supercapacitors.

2. Experimental

Synthesis of the TiO_2 nanobelt arrays (TiO_2 NBs)

All chemicals used in this study were of analytical grade and used without further purification. In a typical experiment, the fabrication process of the TiO_2 nanobelts on the Ti foils was as follows: first, the Ti foils (99.7% purity, 0.25 mm thickness, Sigma-Aldrich) were cut into small pieces (1.5 × 4.0 cm) and sonicated in acetone, ethanol, and deionized water for 10 min, respectively. Then they were put into 40 mL of 5 M NaOH aqueous solution in a 50 mL Teflon-lined autoclave. The autoclave was kept at 180 °C for 24 h. After the autoclave was cooled down naturally to room temperature, the samples were removed, washed with deionized water several times and dried at 60 °C for 10 min in a dry cabinet. Then the samples were immersed in 1.2 M HCl solution for 2 h in order to exchange the Na^+ with H^+. Finally, the as-prepared samples were annealed at 450 °C for 1 h in an electronic furnace to get TiO_2.

Synthesis of the TiO_2@MnO_2 core–shell nanobelt arrays (TiO_2@MnO_2 NBAs)

The TiO_2@MnO_2 NBAs were prepared using a hydrothermal growth method. To grow MnO_2 on TiO_2, the TiO_2 nanobelt array was first coated with a thin layer of amorphous carbon as the sacrificial layer by immersing the TiO_2 NBs into a 0.04 M glucose ethanol solution for 24 h, and followed by carbonization at 450 °C in Ar gas for 2 h. After that, the nanobelt arrays were transferred into a Teflon-lined stainless steel autoclave containing a 0.03 M $KMnO_4$ solution and heated at 160 °C for 5 h. Finally, the sample was removed, washed with distilled water, and dried at 60 °C to obtain the TiO_2@MnO_2 hybrid arrays. For comparison, similar procedures were conducted for 3 h to 5 h to investigate the effect of reaction time.

Characterization

The crystalline structure and phase purity of the TiO_2 NBs and TiO_2@MnO_2 NBAs were identified using X-ray diffraction (XRD) using a D8 Advance (Germany, Bruker) automated X-ray

diffractometer system with Cu-Kα (λ = 1.5406 Å) radiation at 40 kV and 40 mA ranging from 20° to 80° at room temperature. The morphology of the synthesized TiO_2 NBs and TiO_2@MnO_2 NBAs was characterized using scanning electron microscopy (SEM) using a JEOL JSM 6700F microscope (Japan) and transmission electron microscopy (TEM). Raman spectra were carried out using a WITEC CRM200 Raman system equipped with a 532 nm laser source and a 50× objective lens. X-ray photoelectron spectroscopy (XPS) spectra were measured on a Perkin-Elmer model PHI 5600 XPS system with a resolution of 0.3–0.5 eV from a monchromated aluminum anode X-ray source.

Electrochemical evaluation

Electrochemical measurements were carried out using an electrochemical workstation (CHI 760C, CH Instruments Inc., Shanghai) using a three-electrode configuration in 1 M Na_2SO_4 aqueous solution. Both the pristine TiO_2 NBs and hybrid TiO_2@MnO_2 NBAs on Ti foils ($\approx$1.5 × 2.0 cm^2; TiO_2 mass $\approx$ 4.2 mg, MnO_2 mass $\approx$ 1.8 mg) were directly used as the working electrode. The value of specific capacitance (F g^{-1}) and current rate (A g^{-1}) was calculated based on the total mass of the active materials (MnO_2 and TiO_2), and the small contribution from the Ti foil was subtracted. The reference and counter electrodes were Ag/AgCl (sat. KCl) and platinum foil, respectively. Electrochemical impedance spectroscopy (EIS) tests and cyclic voltammetry (CV) measurements were performed on a CHI 760C electrochemical workstation (CH, Shanghai). The EIS measurements were performed by applying an alternate current (AC) voltage with 5 mV amplitude in a frequency range from 0.01 Hz to 100 kHz. CV measurements were performed at a scanning rate of 5–200 mV s^{-1} from −0.2 to 0.8 V at room temperature. Galvanostatic charge–discharge measurements were carried out from −0.2 to 0.8 V at a current density of 200–2000 mA g^{-1}, under an open circuit potential. The specific capacitances were calculated according to equation $C = (I\Delta t)/(\Delta V \times m)$, where I is the constant discharge current, Δt is the discharge time, ΔV is the voltage drop upon discharging (excluding the IR drop), and m is the total mass of the active substance of the electrode material.

3. Results and discussion

A schematic illustration of the fabrication process and optical images of TiO_2@MnO_2 NBAs on the Ti foil substrate are displayed in Fig. 1. It can be seen that the whole process involves three steps: first, TiO_2 NBs were longitudinally grown from the Ti foil substrate *via* a facile modified hydrothermal process plus an ion exchange process according to our previous work;[33] second, the obtained TiO_2 NBs were then subjected to impregnation with glucose aqueous solution and

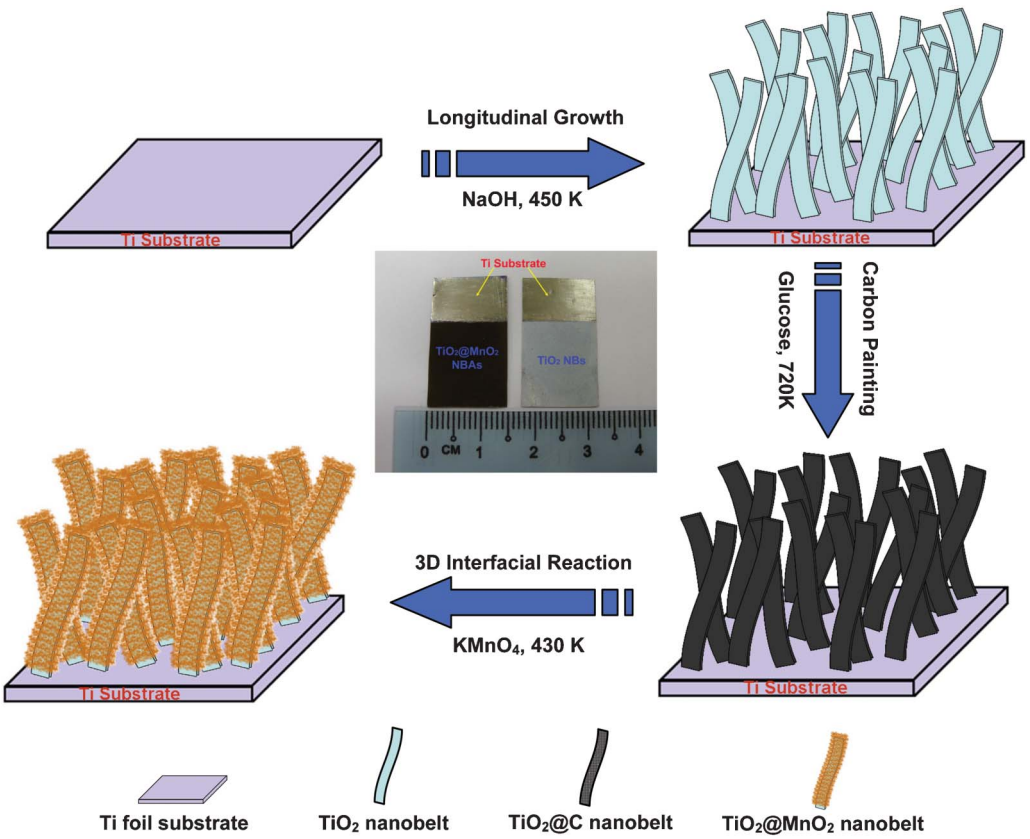

Fig. 1 Schematic mechanism for the direct growth process of TiO_2@MnO_2 core–shell nanobelt arrays on a Ti substrate. The inset shows an optical image of the TiO_2 NBs and TiO_2@MnO_2 NBAs on the Ti foil substrate.

subsequent post-annealing in Ar atmosphere, which leads to the uniform coating of an amorphous carbon layer on the nanobelt surface. The carbon layer here is purposely introduced as an interfacial reactive template for growing the MnO_2 nanostructures. This is encouraged by the fact that MnO_2 can be produced by the green reaction between $KMnO_4$ and carbonaceous materials, such as graphite, carbon nanotubes and graphene, in the absence of any acid or base even at room temperature ($4MnO_4^- + 3C + H_2O = 4MnO_2 + CO_3^{2+} + 2HCO_3^-$).[34–36] Here, we have extended this reaction to a 3D ordered interface by using amorphous carbon, which is more easily generated on a large scale. The carbon coating determines the MnO_2 growth reaction on the surface of the nanobelts, giving rise to well-constructed hybrid architectures. Without carbon, no MnO_2 can be observed on the nanobelts. Before the MnO_2 growth, the sample of the TiO_2 NBs on Ti foil has a grey colour. After MnO_2 deposition, the colour darkened, indicating the uniform formation of MnO_2 ultrathin nanoflakes on the surface of the TiO_2 nanobelts.

The results of the XRD patterns of the as-prepared TiO_2 NBs and the TiO_2@MnO_2 NBAs obtained at different growth stages are shown in Fig. 2. Except for the peaks originating from the Ti substrate, almost all the identified peaks can be perfectly indexed to anatase TiO_2 (JCPDS card no. 21-1272)[37] and MnO_2 (JCPDS card no. 50-0866)[33], indicating the products are the mixture of TiO_2 and MnO_2 or TiO_2@MnO_2 core–shell nanostructures. Among these patterns, the sharp and strong peaks for the as-prepared anatase TiO_2 attest the good crystallinity and high purity of the product. After MnO_2 growth (Fig. S1, ESI†), it can be seen that almost all the diffraction peak positions of the TiO_2 didn't change, only the intensities and sharpness of the diffraction peaks change with reaction time, indicating that the growth time determines the thickness of the MnO_2 shell on the surface of the TiO_2 nanobelts. In respect of the control of the MnO_2 coating process, the optimal reaction time is approximately five hours.

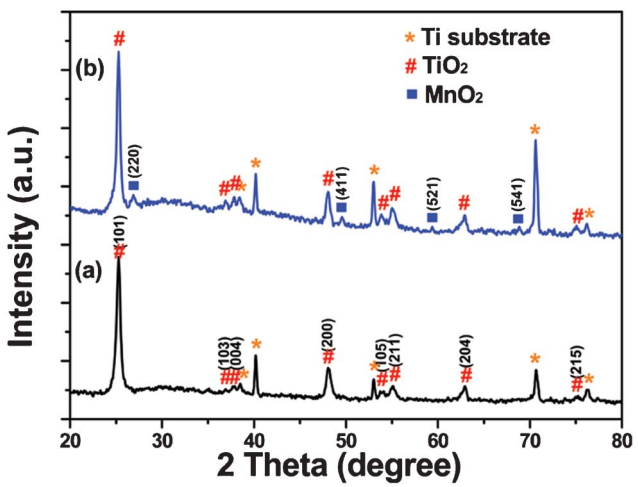

Fig. 2 XRD patterns of as-prepared TiO_2 NBs (curve a), and TiO_2@MnO_2 NBAs obtained after 5 h of growth (curve b).

The SEM images of the TiO_2 NBs and TiO_2@MnO_2 NBAs at different magnifications are shown in Fig. 3. The top-view and cross-sectional images (Fig. 3a–c) of the as-obtained products show that TiO_2 nanobelts longitudinally grow from the Ti foil with well-aligned and uniform characteristics. The enlarged image (inset of Fig. 3a) shows that the TiO_2 nanobelt has a relatively smooth surface. Close observation reveals that an individual TiO_2 nanobelt is typically about 6–10 μm in length, 300–500 nm in width, and 20–40 nm in thickness (Fig. S1, ESI†). After MnO_2 growth, the surface of TiO_2 was homogeneously covered with a layer of dense MnO_2 ultrathin nanoflakes as shown in Fig. 3d–f. The interconnected MnO_2 nanoflakes create a highly porous surface morphology. This configuration can provide an especially high surface area and more active sites for the adsorption of Na^+, which hence endows the MnO_2 with a very high specific capacitance. As shown in Fig. S1, ESI,†aligned nanobelt arrays are preserved after carbon painting (Fig. S1a, ESI†) and their compositions are confirmed by the Raman spectrum (Fig. S1b, ESI†). In addition to the five peaks from the TiO_2, peaks at 1340 cm^{-1} (D band) and 1590 cm^{-1} (G band) are observed and demonstrate the successful introduction of amorphous carbon. After a 3 h hydrothermal reaction, the TiO_2 nanobelts' surfaces become rough, decorated by many tiny MnO_2 "buds" (SEM; Fig. S1c–e, ESI†), which distinctly indicates that the MnO_2 nanoflakes grow on the surface of the TiO_2 nanobelts. Ultrathin (<10 nm) MnO_2 nanoflakes formed uniformly on the nanobelt surface can be observed after 5 h complete reaction between $KMnO_4$ and carbon, as displayed in Fig. S2d,e, ESI†.

The structures of the nanobelts were further investigated using TEM at different magnifications. The low-magnification TEM image in Fig. 4a,b clearly shows that an individual TiO_2 nanobelt has a diameter about 400 nm (~500 nm), and its corresponding high-magnification TEM image taken near the edge is shown in Fig. 4c. A lattice spacing of 0.19 nm is recognized and can be ascribed to the (200) planes of anatase TiO_2. The selected area electron diffraction (SAED) pattern of the TiO_2 nanobelt shows a set of well-defined spots, indicative of the single-crystallinity. The low-magnification TEM image of the MnO_2 nanoflakes on the surface of TiO_2 nanobelt is shown in Fig. 4d,e. It can be seen that the MnO_2 nanoflakes fully cover the TiO_2 nanobelt surface. This core–shell composite nanostructure is expected to achieve high performance in a supercapacitor: the ultrathin MnO_2 shell is beneficial to the fast faradic reaction, which would enable high specific capacitance, and the TiO_2 nanobelt core serves as a fast path for electron transport, which would enable high power density. The advantages will be discussed in detail in the following paragraph. In addition, the SAED pattern was also obtained to investigate the crystalline characteristics of the TiO_2@MnO_2 nanobelt based on the selected area shown in the inset of Fig. 4f. Clear lattice fringes were also observed (as shown in Fig. 4d), further demonstrating the superior crystal quality of TiO_2@MnO_2 NBAs.

Raman spectra of the TiO_2@MnO_2 NBAs investigated at different growth stages clearly reveal the composition evolu-

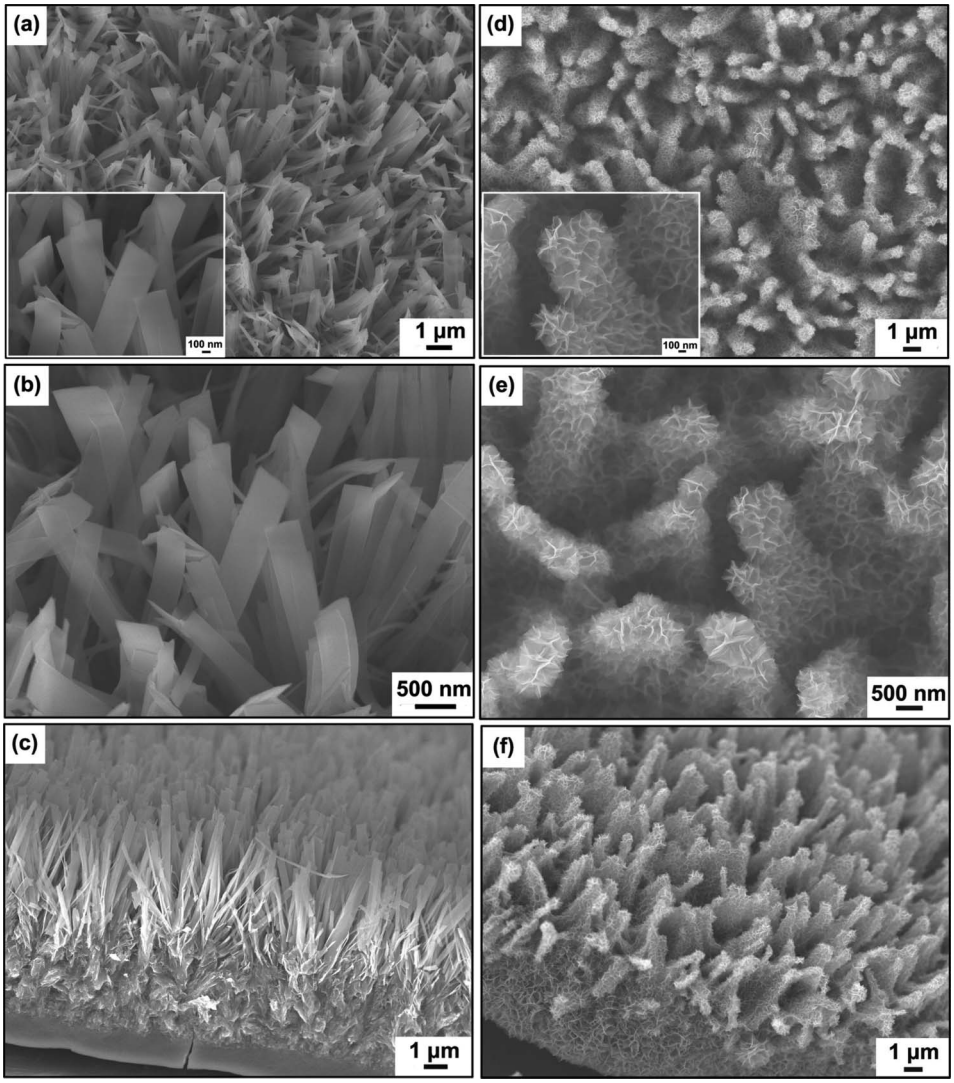

Fig. 3 (a,b) Low-magnification and enlarged SEM images of the TiO_2 NBs; (c) Cross-sectional SEM image of the TiO_2 NBs; (d,e) Low-magnification and enlarged SEM images of the TiO_2@MnO_2 NBAs; (f) Cross-sectional SEM image of the TiO_2@MnO_2 NBAs.

tion process (see Fig. 5). For the TiO_2 nanobelt arrays (Fig. 5a), there are six Raman active modes (A_{1g} + $2B_{1g}$ + $3E_g$), which appear at 149 cm^{-1} (E_g), 196 cm^{-1} (E_g), 393 cm^{-1} (B_{1g}), 513 cm^{-1} (A_{1g}), 519 cm^{-1} (B_{1g}), and 636 cm^{-1} (E_g), respectively. They are similar to the Raman spectrum of the anatase TiO_2, and consistent with the previous report of Ohsaka.[38,39] The strongest E_g mode at 149 cm^{-1} arising from the external vibration of the anatase structure is well resolved, indicating the formation of the anatase phase,[34] which is consistent with the XRD result shown in Fig. 2. The TiO_2@MnO_2 NBAs exhibit three distinct Raman peaks, at 494, 575, and 655 cm^{-1}, respectively, which can be assigned to oxygen vibrations of the tunnel α-MnO_2 structure.[40,41]

X-ray photoelectron spectroscopy (XPS) was carried out to check the surface chemical composition, purity, and the oxidation valence states of the TiO_2@MnO_2 NBAs after 3 h and 5 h of growth, respectively (the results are shown in Fig. 6). The survey scan spectrum shows that there are five elements (Mn, Ti, O, C and K) existing on the surface of the sample after 3 h of growth. However, Ti is not found in the sample after 5 h of growth, probably because the MnO_2 layer is too thick. The presence of the carbon peak indicates that the amorphous carbon coating on the TiO_2 nanobelt surface was not fully involved in the interfacial reaction, and the presence of a potassium peak indicates that pure TiO_2 NBs and TiO_2@MnO_2 NBAs were both completely doped with K^+ (shown in the ESI† Fig. S4). The deconvolution peak of the O 1s spectrum can be resolved into two components of 530 and 531.3 eV, respectively (see Fig. 6b). The low binding energy component at 530 eV is attributed to the O^{2-} bond with titanium and manganese, the latter peak is assigned to OH^-.[11,34,42,43] Fig. 6c presents the XPS spectra of the Ti 2p doublet peaks, the binding energy of Ti $2p_{1/2}$ and Ti $2p_{3/2}$ was observed at approximately 464.5 eV and 458.7 eV, respectively. The split between the Ti $2p_{1/2}$ and Ti $2p_{3/2}$ core levels is 5.8 eV, indicating a normal state of Ti^{4+} in the anatase TiO_2. Similarly, the core level spectra of Mn 2p

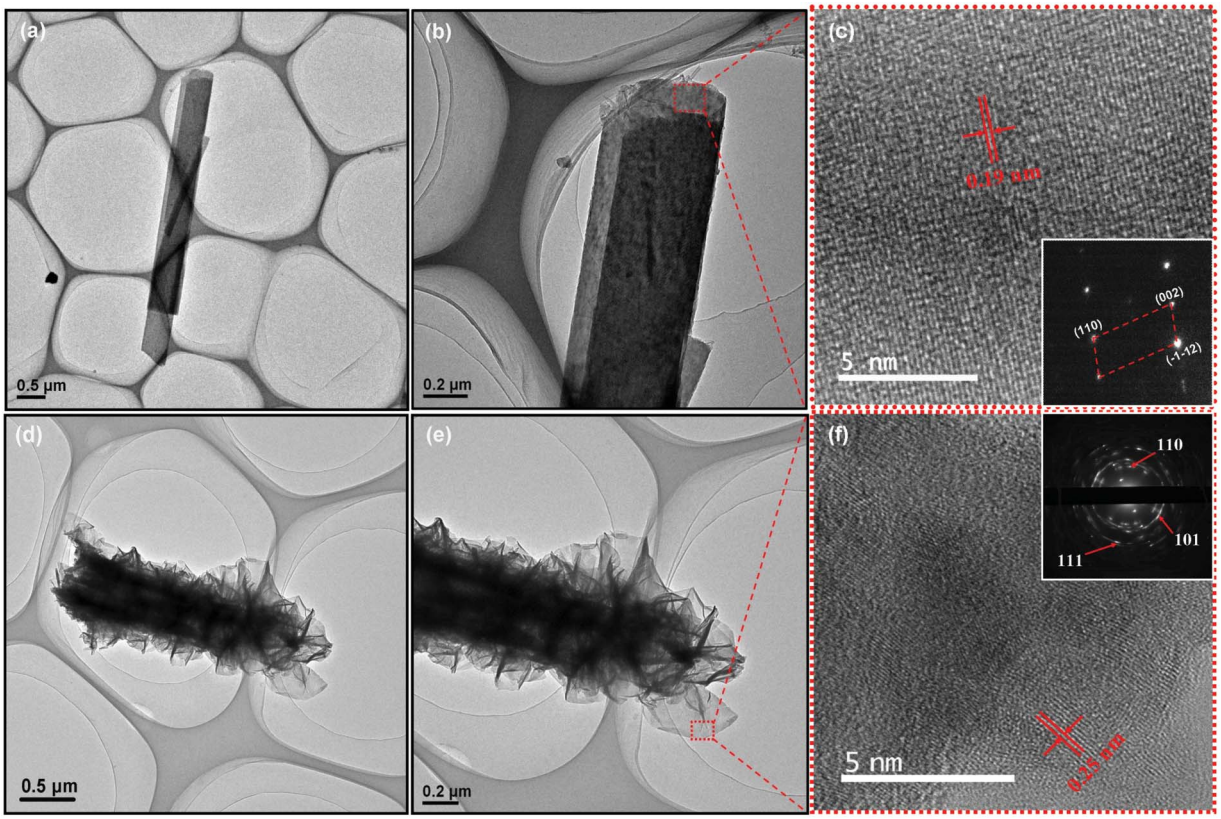

Fig. 4 (a,b,c) Low-magnification and high-magnification TEM images of the TiO_2 NBs; (d,e,f) Low-magnification and high-magnification TEM images of the TiO_2@MnO_2 NBAs. The insets of (c) and (f) are the corresponding SAED patterns from the TiO_2 NBs and TiO_2@MnO_2 NBAs respectively.

were fitted and are shown in Fig. 6d. Two peaks located at *ca.* 642.4 and 654.7 eV are observed with a spin-energy separation of 12.3 eV, which can be attributed to the Mn $2p_{3/2}$ and Mn $2p_{1/2}$ binding energies, respectively.[33,44] Herein, the result clearly indicates that a certain degree of oxidation occurred during the preparation of the TiO_2@MnO_2 NBAs. It is well-known that potassium permanganate ($KMnO_4$) is a strong oxidant. Some carboxylic acid groups as well as other oxygenated functional groups can be expected on the carbon fibers' surfaces after immersing the carbon fibers in $KMnO_4$ solution at elevated temperatures.

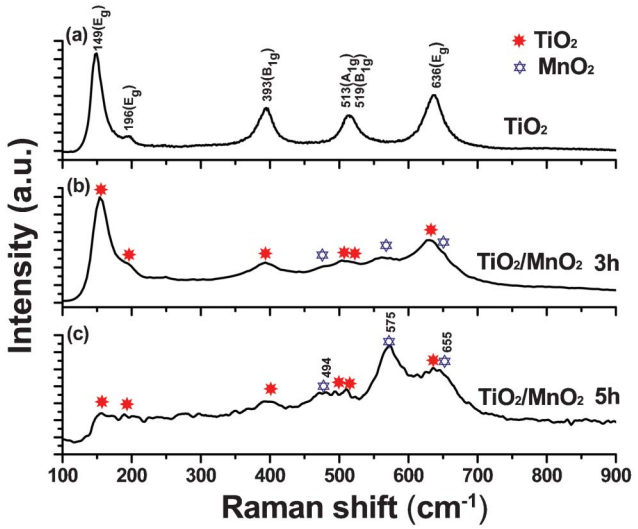

Fig. 5 (a) Raman spectra of the pure TiO_2 NBs; (b,c) Raman spectra of the TiO_2@MnO_2 NBAs obtained after 3 h and 5 h of growth, respectively.

To investigate the advantages of the unique TiO_2@MnO_2 NBAs as the electrodes for supercapacitor devices, electrochemical tests were carried out in a three-electrode configuration with a Pt foil as counter electrode and Ag/AgCl as the reference electrode in an electrolyte of 1 M Na_2SO_4 aqueous solution. In addition, the electrochemical performance of the TiO_2 NBs electrodes was also tested (as shown in Fig. S5, ESI†). Fig. 7a shows the CV curves of the TiO_2@MnO_2 NBAs electrodes at scan rates of 5–200 mV s^{-1}. The CV curves at high scan rates are not perfectly rectangular. The specific capacitance of the electrode was calculated from the CV curves according to the following equation,

$$C = Q/(\Delta V \times \Delta m) \quad (1)$$

where C (F g^{-1}), Δm (g), Q (C), ΔV (V) are the specific capacitance, mass of the active materials (or mass of the total electrode materials), average charge during the charging and discharging process, and the potential window, respectively.[26]

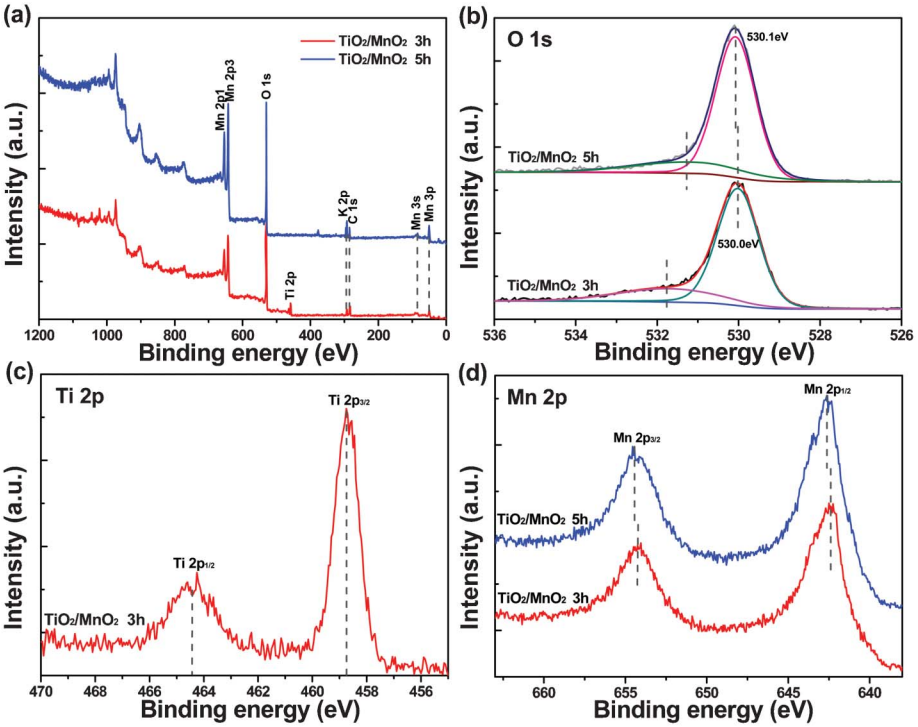

Fig. 6 (a) Survey XPS spectrum; (b) O 1s XPS spectra; (c) Ti 2p XPS spectra and (d) Mn 2p XPS spectra for the TiO_2@MnO_2 NBAs obtained after 3 h and 5 h of growth, respectively.

The areas surrounded by the CV curves are not significantly influenced by changing the scan rates, implying the sample has good rate capability. For comparison, the CV curves of the pristine Ti foil substrate, TiO_2 NBs, and TiO_2@MnO_2 NBAs at 100 mV s^{-1} are also shown in Fig. 7b. It can be found that the current density of the TiO_2@MnO_2 NBAs at the same scan rate is higher than that for other two electrodes. It is noteworthy that the capacitance contribution from the Ti foil substrate is negligible. The significant increase of the CV integrated area suggests that the flake-like MnO_2 nanostructures have a much higher specific capacitance, which will be discussed. The excellent electrochemical capability of the TiO_2@MnO_2 NBAs must be attributed to their unique microstructure and the synergetic effect from the ultrathin MnO_2 nanoflake shell and the TiO_2 nanobelt core. It is obvious that the MnO_2 nanoflakes are well grown and dispersed on the surface of the TiO_2 nanobelts, which will enhance the electrochemical kinetics of the material. The interconnected MnO_2 nanoflakes create a highly porous surface morphology, as well as an ordered array geometry, which can provide higher surface area and more active sites for the rapid intercalation of cations (Na^+) into the electrode during reduction and deintercalation processes.[15,39,42] In order to further evaluate the electrochemical performance of the as-prepared TiO_2@MnO_2 NBAs composites at different current densities in 1 M Na_2SO_4 aqueous solution, constant current charge–discharge measurements were carried out, and the results are shown in Fig. 7c. It can be seen that all the curves are highly linear and consistent at various current densities from 200 to 2000 mA g^{-1}. This implies that the electrode has excellent electrochemical reversibility and charge-discharge properties. Furthermore, the specific capacitance can be calculated from the discharge curves according to the above mentioned equations. On the basis of the above results, the specific capacitance of the TiO_2@MnO_2 NBAs at 200, 300, 500, 800, 1000 and 2000 mA g^{-1} is 454.6, 336, 242.5, 160, 128.4 and 54 F g^{-1}, respectively. These results can be ascribed to the discrepant insertion–deinsertion behaviors of cations (Na^+) from the electrolyte to MnO_2.[33,39] It is emphasized that the specific capacitance is calculated according to the mass of the active materials (TiO_2 mass + MnO_2 mass), and Ti substrate is not included for this calculation. The specific capacitance based on the mass of the active materials *versus* current density is also shown in Fig. 7d.

The long-term cycle stability of supercapacitors is another critical requirement for their practical applications. The cycling lifetime tests over 3000 cycles for both the hybrid TiO_2@MnO_2 NBAs and pristine TiO_2 NBs were carried out at 200 mV s^{-1} and the results are shown in Fig. 8a. It is found that the hybrid TiO_2@MnO_2 NBAs electrode exhibits a good long-term electrochemical stability, and the capacitance loss after 3000 cycles is only 13.7%. By contrast, only 84.2% capacitance was retained for the pristine TiO_2 NBs. In addition, the stable charge–discharge curve of the last 21 cycles at 3 Ag^{-1} for TiO_2@MnO_2 NBAs is also shown in Fig. 8b. The result shows that the charge curves are still quite symmetric to their corresponding discharge counterparts, indicating no significant structural change of the TiO_2@MnO_2 NBAs electrode during the charge–discharge

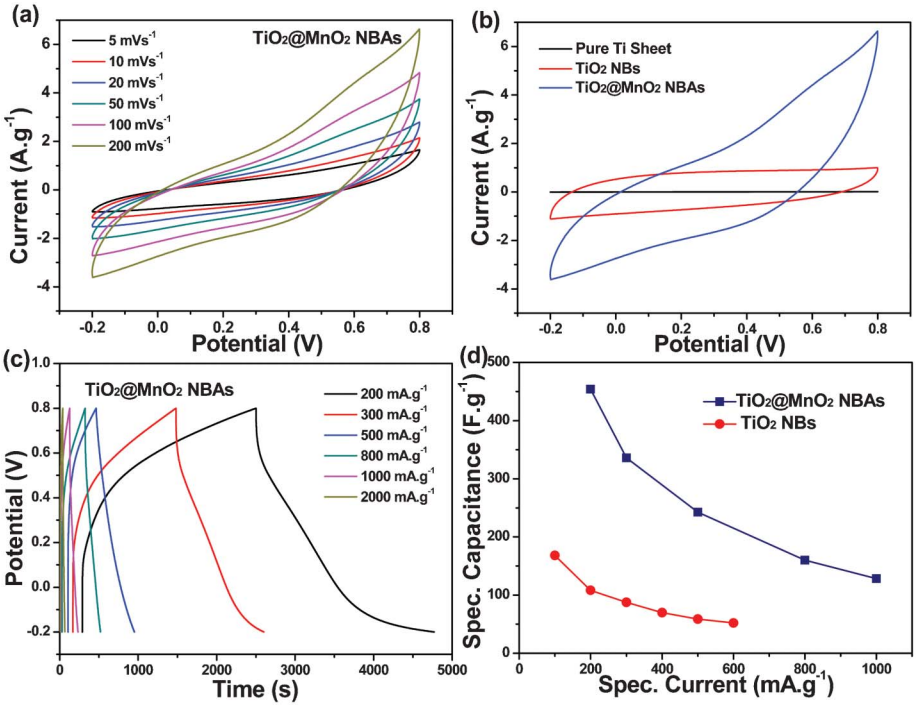

Fig. 7 (a) Cyclic voltammograms of TiO_2@MnO_2 NBAs at different scan rates; (b) Cyclic voltammograms of the different electrode materials at 200 mV s^{-1}; (c) Charge–discharge curves of the TiO_2@MnO_2 NBAs at various current densities; (d) Current density dependence of the specific capacitance of the TiO_2@MnO_2 NBAs (blue curve) and TiO_2 NBs (red curve).

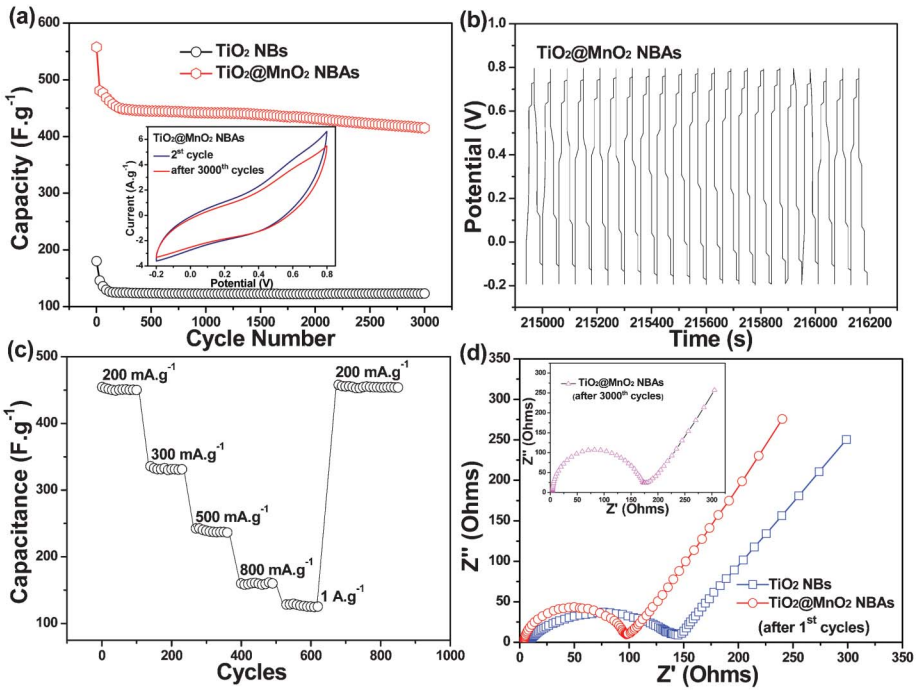

Fig. 8 (a) Cycling performance of the TiO_2@MnO_2 NBAs supercapacitor device over 3000 cycles (inset: comparison of the CV curves between 2nd cycles and after the 3000th cycles for a charge–discharge test at 3 A g^{-1}); (b) The charge–discharge curve of the last 21 cycles at 3 A g^{-1} during 3000 cycles for the TiO_2@MnO_2 NBAs; (c) Cycling stability of the TiO_2@MnO_2 NBAs at various current densities; (d) Electrochemical impedance spectra after the 1st cycles of the TiO_2 NBs and TiO_2@MnO_2 NBAs electrodes (inset: electrochemical impedance spectra after the 3000th cycle of the TiO_2@MnO_2 NBAs electrodes).

processes. Such excellent cycling stability is mainly attributed to the porous configuration of the TiO_2 core, which can not only lead to more contact area with the electrolyte, but also can accommodate the possible volume change during cycling process. More significantly, the synergistic effect between MnO_2 and TiO_2 mentioned above may inhibit the anodic dissolution of MnO_2, and consequently improve the electrochemical reversibility and stability of the hybrid electrode.[45,46] After long-term cycling, the TiO_2@MnO_2 NBAs nanostructures are well maintained and preserved overall with little structural deformation after 3000 cycles as verified in the inset of Fig. 8a.

The combination of MnO_2 and TiO_2 with a unique morphology and independent electro-activities into a single engineered hierarchical architecture can substantially enhance their electrochemical properties. The shell material was an active material while the core material served as the nanobelt current collector. It is believed that the synergistic contribution from ultrathin MnO_2 nanoflakes, the single-crystalline TiO_2 nanobelts, and the ordered array configuration should account for the good cycle performance and rate capability (as shown in Fig. S3, ESI†). First, by growing directly from the TiO_2 nanobelt scaffold, the surfaces of the MnO_2 nanoflakes are well separated, making them fully available to the Na^+ in the electrolyte. This is in distinct contrast to most MnO_2-based electrode systems, in which the nanosized active sites were largely hindered by numerous unwanted interfaces.[40,47] The entirely exposed nanoflake edges can also facilitate the fast Na^+ intercalation into the layered structure, thus enhancing the electrochemical kinetics. Second, ultrathin MnO_2 nanoflakes construct a three dimensional (3D) and highly porous structure on the surface of the TiO_2 nanobelts. Even completely covered, the TiO_2 core nanobelts can still be accessed by OH^- and initiate the redox reaction (Fig. S3, ESI:†similar diffusion resistance is observed for the TiO_2@MnO_2 NBAs and the pristine TiO_2 NBs). It is worth noting that the porous structure of the TiO_2 nanobelts would further increase the electrolyte–material contact area and enhance ion diffusion, which is very critical to high-power energy storage. Furthermore, the array directly grown on the Ti foil substrate can ensure good mechanical adhesion and electrical connection to the current collector,[48] avoiding the use of polymer binders and conductive additives, which generally add extra contact resistance or weight. After long-term cycling, the hierarchical structure of the hybrid nanobelts array is preserved overall with little structural deformation, as illustrated in Fig. S2f, ESI.†

To further demonstrate the advantage of the synergistic effects in this electrode design, the cycling performance of the hybrid TiO_2@MnO_2 NBAs at progressively increased current density was recorded in Fig. 8c. The hybrid structure exhibits stable capacitance at different current densities. During the first 100 cycles with a charge–discharge density of 200 mA g^{-1}, the hybrid structure shows a cycle stability performance of about 450 F g^{-1}. In the following 400 cycles, the charge–discharge rate changes successively. After 500 cycles, with the current rate being again decreased back to 200 mA g^{-1} for another 200 cycles, a capacitance of about 454 Fg^{-1} can be recovered and without noticeable decrease, which demonstrates that the hybrid structure has excellent rate performance and cycling ability. This result highlights the capability of the 3D pseudocapacitive material-based hybrid array electrode to meet the requirements of both long cycle lifetime and good rate capability, which are important merits for practical energy storage devices.

Electrochemical impedance spectroscopy (EIS) has been recognized as a complementary technique to galvanostatic cyclic voltammetry which can provide more information on the electrochemical frequency behavior of electrode materials for supercapacitors. To gain further insight into the advantages of these electrodes, impedance spectra of the pristine TiO_2 NBs and TiO_2@MnO_2 NBAs composite after the 1st cycle and 3000th cycle were measured in the frequency range from 0.01 Hz to 100 kHz at an open circuit potential with an AC perturbation of 5 mV. The result shows that the Nyquist plots are in the form of an arc at the high frequency region and a straight 45° sloped line at low frequency region. The arc in the high frequency region is associated with the interfacial properties of the electrodes and corresponds to the charge-transfer resistance, and the straight line in the low frequency region is ascribed to the diffusive resistance related to the diffusion of the electrolyte within the pores of the electrode. It is obvious that both the TiO_2@MnO_2 NBAs and the pristine TiO_2 NBs have similar diffusion resistance, but the TiO_2@MnO_2 NBAs demonstrate a relatively smaller charge transfer resistance. As shown in the inset of Fig. 8d, the arc increment from the 1st to the 3000th cycles is not so obvious indicating that the TiO_2@MnO_2 NBAs nanostructures are well maintained and preserved overall with little structural deformation after 3000 cycles, which can also be verified by the SEM images in Fig. S2f, ESI.†

Power density and energy density are also important parameters for the investigation of the electrochemical performance of electrochemical capacitors. They have been calculated according to the following equations and the results are listed in Table 1 (as shown in the ESI†):

$$E = \frac{1}{2} C(\Delta V)^2 \quad (2)$$

$$P = E/\Delta t \quad (3)$$

where P (kW kg^{-1}) is the power density, C (F g^{-1}) is the specific capacitance, ΔV (V) is the potential window of the discharge process, Δt (s) is the discharge time, and E (W h kg^{-1}) is the energy density.[25] Based on the mass of the active material, the energy density and power density could reach 7.5 W h kg^{-1} and 1 kW kg^{-1} at 2 A g^{-1}, respectively. These results suggest that the TiO_2@MnO_2 NBAs composite is a very promising electrode material for fabricating supercapacitors.

4. Conclusions

In summary, we have demonstrated a new, facile, and cost-efficient strategy towards the synthesis of a TiO_2 nanobelt core and MnO_2 nanoflake shell hierarchical nanostructure, and the application of these composites as the electrodes for supercapacitor has been investigated. Due to their rationally designed unique structure, and the smart hybridization of MnO_2 and TiO_2, the electrodes exhibit a high specific capacitance of 454 F g^{-1} at 200 mA g^{-1} with an excellent cycling stability. The strategy used here could be extended to the other materials and the idea of hybridizing two materials together could create new opportunities in other areas.

Acknowledgements

This work is supported by the Singapore National Research Foundation under NRF RF Award No. NRF-RF2010-07.

Notes and references

1 G. H. Yu, L. B. Hu, M. Vosgueritchian, H. L. Wang, X. Xie, J. R. McDonough, X. Cui, Y. Cui and Z. N. Bao, *Nano Lett.*, 2011, **11**, 2905.
2 Y. S. Luo, J. S. Luo, J. Jiang, W. W. Zhou, H. P. Yang, X. Y. Qi, H. Zhang, H. J. Fan, D. Y. W. Yu, C. M. Li and T. Yu, *Energy Environ. Sci.*, 2012, **5**, 6559.
3 P. Simon and Y. Gogotsi, *Nat. Mater.*, 2008, **7**, 845.
4 G. P. Wang, L. Zhang and J. J. Zhang, *Chem. Soc. Rev.*, 2012, **41**, 797.
5 Y. Hou, Y. W. Cheng, T. Hobson and J. Liu, *Nano Lett.*, 2010, **10**, 2727.
6 A. S. Arico, P. Bruce, B. Scrosati, J. M. Tarascon and W. V. Schalkwijk, *Nat. Mater.*, 2005, **4**, 366.
7 A. L. M. Reddy, M. M. Shaijumon, S. R. Gowda and P. M. Ajayan, *Nano Lett.*, 2009, **9**, 1002.
8 R. Kötz and M. Carlen, *Electrochim. Acta*, 2000, **45**, 2483.
9 H. L. Wang, Q. L. Hao, X. J. Yang and L. D. Lu, *Electrochem. Commun.*, 2009, **11**, 1158.
10 C. C. Hu, K. H. Chang, M. C. Lin and Y. T. Wu, *Nano Lett.*, 2006, **6**, 2690.
11 J. P. Liu, J. Jiang, C. W. Cheng, H. X. Li, J. X. Zhang, H. Gong and H. J. Fan, *Adv. Mater.*, 2011, **23**, 2076.
12 R. Liu and S. B. Lee, *J. Am. Chem. Soc.*, 2008, **130**, 2942.
13 H. Jiang, L. P. Yang, C. Z. Li, C. Y. Yan, P. S. Lee and J. Ma, *Energy Environ. Sci.*, 2011, **4**, 1813.
14 W. F. Wei, X. W. Cui, W. X. Chen and D. G. Ivey, *Chem. Soc. Rev.*, 2011, **40**, 1697.
15 H. Jiang, C. Z. Li, T. Sun and J. Ma, *Chem. Commun.*, 2012, **48**, 2606.
16 W. F. Wei, X. W. Cui, W. X. Chen and D. G. Ivey, *Chem. Soc. Rev.*, 2011, **40**, 1697.
17 W. B. Yan, T. Ayvazian, J. Y. Kim, Y. Liu, K. C. Donavan, W. D. Xing, Y. A. Yang, J. C. Hemminger and R. M. Penner, *ACS Nano*, 2011, **5**, 8275.
18 S. W. Lee, B. M. Gallant, H. R. Byon, P. T. Hammond and S. H. Yang, *Energy Environ. Sci.*, 2011, **4**, 1972.
19 H. Kim and B. N. Popov, *J. Electrochem. Soc.*, 2003, **150**, D56.
20 A. S. Arico, P. Bruce, B. Scrosati, J.-M. Tarascon and W. V. Schalkwijk, *Nat. Mater.*, 2005, **4**, 366.
21 V. Etacheri, R. Marom, R. Elazari, G. Salitra and D. Aurbach, *Energy Environ. Sci.*, 2011, **4**, 3243.
22 M. V. Reddy, T. Yu, C. H. Sow, Z. X. Shen, C. T. Lim, G. V. S. Rao and B. V. R. Chowdari, *Adv. Funct. Mater.*, 2007, **17**, 2792.
23 Y. G. Guo, Y. S. Hu, W. Sigle and J. Maier, *Adv. Mater.*, 2007, **19**, 2087.
24 Y. L. Chueh, C. H. Hsieh, M. T. Chang, L. J. Chou, C. S. Lao, J. H. Song, J. Y. Gan and Z. L. Wang, *Adv. Mater.*, 2007, **19**, 143.
25 J. Yan, E. Khoo, A. Sumboja and P. S. Lee, *ACS Nano*, 2010, **4**, 4247.
26 A. Magasinski, P. Dixon, B. Hertzberg, A. Kvit, J. Ayala and G. Yushin, *Nat. Mater.*, 2010, **9**, 353.
27 L. Mai, L. Xu, C. Han, X. Xu, Y. Luo, S. Zhao and Y. Zhao, *Nano Lett.*, 2010, **10**, 4750.
28 J. S. Chen, Y. L. Tan, C. M. Li, Y. L. Cheah, D. Luan, S. Madhavi, F. Y. C. Boey, L. A. Archer and X. W. Lou, *J. Am. Chem. Soc.*, 2010, **132**, 6124.
29 X. S. Fang, L. F. Hu, K. F. Huo, B. Gao, L. J. Zhao, M. Y. Liao, P. K. Chu, Y. Bando and D. Golberg, *Adv. Funct. Mater.*, 2011, **21**, 3907.
30 J. Jiang, J. P. Liu, W. W. Zhou, J. H. Zhu, X. T. Huang, X. Y. Qi, H. Zhang and T. Yu, *Energy Environ. Sci.*, 2011, **4**, 5000.
31 Y. Y. Lu, F. Zhang, Y. Q. Dou, Y. P. Zhai, J. X. Wang, H. J. Liu, Y. Y. Xia, B. Tu and D. Y. Zhao, *J. Mater. Chem.*, 2012, **22**, 93.
32 Y. S. Luo, J. S. Luo, W. W. Zhou, X. Y. Qi, H. Zhang, Y. W. Y. Denis, C. M. Li, H. J. Fan and T. Yu, *J. Mater. Chem. A*, 2013, **1**, 273.
33 Y. S. Luo, J. Jiang, W. W. Zhou, H. P. Yang, J. S. Luo, X. Y. Qi, H. Zhang, D. Y. W. Yu, C. M. Li and T. Yu, *J. Mater. Chem.*, 2012, **22**, 8634.
34 X. Jin, W. Zhou, S. Zhang and G. Z. Chen, *Small*, 2007, **3**, 1513.
35 S. W. Lee, J. Kim, S. Chen, P. T. Hammond and S. H. Yang, *ACS Nano*, 2010, **4**, 3889.
36 J. Yan, Z. J. Fan, T. Wei, W. Z. Qian, M. L. Zhang and F. Wei, *Carbon*, 2010, **48**, 3825.
37 F. F. Cao, X. L. Wu, S. Xin, Y. G. Guo and L. J. Wan, *J. Phys. Chem. C*, 2010, **114**, 10308.
38 H. C. Choi, Y. M. Jung and S. B. Kim, *Vib. Spectrosc.*, 2005, **37**, 33.
39 T. Ohsaka, *J. Phys. Soc. Jpn.*, 1980, **48**, 1661.
40 W. F. Zhang, Y. L. He, M. S. Zhang, Z. Yin and Q. Chen, *J. Phys. D: Appl. Phys.*, 2000, **33**, 912.
41 C. M. Julien, M. Massot and C. Poinsignon, *Spectrochim. Acta, Part A*, 2004, **60**, 689.
42 V. Subramanian, H. W. Zhu and B. Q. Wei, *J. Power Sources*, 2006, **159**, 361.
43 V. Subramanian, H. Zhu, R. Vajtai, P. M. Ajayan and B. Wei, *J. Phys. Chem. B*, 2005, **109**, 20207.
44 M. Toupin, T. Brousse and D. Belanger, *Chem. Mater.*, 2004, **16**, 3184.
45 H. Kim and B. N. Popov, *J. Electrochem. Soc.*, 2003, **150**, D56.
46 Y. S. Chen and C. C. Hu, *Electrochem. Solid-State Lett.*, 2003, **6**, A210.
47 S. H. Kim, Y. I. Kim, J. H. Park and J. M. Ko, *Int. J. Electrochem. Sci.*, 2009, **4**, 1489.
48 J. Jiang, Y. Y. Li, J. P. Liu and X. T. Huang, *Nanoscale*, 2011, **3**, 45.

